ACADÉMIE
DES SCIENCES
INSTITUT DE FRANCE

Comptes Rendus
Mécanique

Paulo Elias Carneiro Pereira, Stanley Washington Ferreira de Rezende, José dos Reis Vieira de Moura Júnior and Roberto Mendes Finzi Neto

SGS method applied to damage location and uncertainty modeling for sensor grid in the ISHM

Volume 352 (2024), p. 19-37

Online since: 1 February 2024

https://doi.org/10.5802/crmeca.239

The Comptes Rendus. Mécanique *are a member of the Mersenne Center for open scientific publishing*
www.centre-mersenne.org — e-ISSN : 1873-7234

ACADÉMIE DES SCIENCES
INSTITUT DE FRANCE

Comptes Rendus. Mécanique
2024, Vol. 352, p. 19-37
https://doi.org/10.5802/crmeca.239

Research article / *Article de recherche*

SGS method applied to damage location and uncertainty modeling for sensor grid in the ISHM

Méthode SGS appliquée à la localisation des dommages et à la modélisation de l'incertitude pour la grille de capteurs dans l'ISHM

Paulo Elias Carneiro Pereira [a,*], **Stanley Washington Ferreira de Rezende** [b], **José dos Reis Vieira de Moura Júnior** [c] **and Roberto Mendes Finzi Neto** [b]

[a] School of Mechanical Engineering, Federal University of Uberlândia, 2121 João Naves de Ávila Av., Uberlândia, Brazil

[b] Mathematics and Technology Institute, Federal University of Catalão, 1120 Dr. Lamartine Pinto de Avelar Av., Catalão, Brazil

E-mails: paulo_elias_carneiro@ufu.br (P. E. C. Pereira), stanley_washington@ufu.br (S. W. F. de Rezende), zereis@ufcat.edu.br (J. R. V. Moura Júnior), finzi@ufu.br (R. M. Finzi Neto)

Abstract. Damage location estimation is a critical aspect of condition-based maintenance systems, particularly in the context of electromechanical impedance monitoring. Various approaches have been developed to estimate damage location, yet they often need more capability to assess the reliability of data collected from sensor grids. In this paper, we introduce a novel method based on Sequential Gaussian Simulation (SGS) to pinpoint damage locations on aluminum plates and create maps that illustrate the spatial uncertainty associated with damage index values throughout the structure. Our proposed approach builds upon the SGS method and encompasses the assessment of four different sensor grid configurations to investigate how sensor spacing affects spatial uncertainty. The findings demonstrate the technique's effectiveness in accurately predicting damage positions. Moreover, by leveraging the uncertainty information generated, we can identify specific areas necessitating careful attention, thus offering valuable insights for optimizing sensor grid design.

Résumé. L'estimation de la localisation des dommages est un aspect critique des systèmes de maintenance basés sur l'état, en particulier dans le contexte de la surveillance de l'impédance électromécanique. Diverses approches ont été mises au point pour estimer la localisation des dommages, mais elles nécessitent souvent davantage de capacités pour évaluer la fiabilité des données collectées à partir des grilles de capteurs. Dans cet article, nous présentons une nouvelle méthode basée sur la simulation gaussienne séquentielle (SGS) pour localiser les dommages sur les plaques d'aluminium et créer des cartes qui illustrent l'incertitude spatiale associée aux valeurs de l'indice de dommage dans l'ensemble de la structure. L'approche proposée s'appuie sur la méthode SGS et englobe l'évaluation de quatre configurations différentes de la grille de capteurs afin d'étudier comment l'espacement des capteurs affecte l'incertitude spatiale. Les résultats démontrent l'efficacité de la technique pour prédire avec précision les positions des dommages. De plus, en exploitant les

* Corresponding author.

informations d'incertitude générées, nous pouvons identifier des zones spécifiques nécessitant une attention particulière, offrant ainsi des indications précieuses pour optimiser la conception de la grille de capteurs.

Keywords. Structural health monitoring, Electromechanical impedance-based method, Damage detection and location, Sequential Gaussian simulation.

Mots-clés. Surveillance de la santé des structures, Méthode basée sur l'impédance électromécanique, Détection et localisation des dommages, Simulation gaussienne séquentielle.

Manuscript received 15 September 2023, revised 22 December 2023 and 11 January 2024, accepted 18 January 2024.

1. Introduction

The Electromechanical Impedance-based Structural Health Monitoring has been used for damage identification in several structures and materials due to being a nondestructive, low-cost method and capable of detecting small-scale phenomena [1, 2].

Several researchers have demonstrated the application of Integrated Structural Health Monitoring (ISHM) effectively. Nomelini *et al.* [3], Maruo *et al.* [4], and Finzi Neto *et al.* [5] successfully employed ISHM for monitoring both aircraft structures and aluminum specimens, yielding promising results. Furthermore, de Rezende *et al.* [6] and Cavalini Jr *et al.* [7] extended the application of impedance-based methods to rotating machines. Their innovative approach involved integrating deep learning models to detect damage present in these systems. These diverse applications encompass a wide range of topics, with many investigations centered explicitly around the crucial stage of damage detection.

However, the description of damage involves more than just identifying it. Determining where the damage is located is crucial so that maintenance efforts can be targeted effectively. Knowing the location helps to make informed decisions about how to proceed with repairs or other interventions.

Researchers have created multiple methods to predict the location of damage in a material. One of these methods, known as the damage index approach, was developed by Kim *et al.* [8]. They conceived a metric that could indicate whether the damage was present and where it was located by combining two measurements: the root-mean-square deviation (RMSD) obtained from impedance-based measurements and the RMSD obtained from guided wave-based measurements. Applying this new index could generate polynomial curves that accurately located debonding in a carbon-fiber-reinforced polymer (CFRP) layer attached to a concrete beam. In their experiments, they found that the peaks of these polynomial curves matched the positions of the debonding in the material.

Cherrier *et al.* [9] employed Inverse Distance Weighting (IDW) to generate damage localization maps for a beam and six plates made of composite material. They assigned weights based on an acoustic attenuation coefficient. Using IDW, the researchers could forecast the probable locations of damage using probability maps. On the other hand, the technique used by Cherrier *et al.* [9] considers that the damage index values are inversely proportional to the damage's distance. Based on this concept, Castro *et al.* [10] developed an algorithm to indicate the probability of damage in each pixel. The resulting probability depends, among others, on the cross-correlation square difference (CCSD) index, weighted by a linear inverse distance between each PZT patch and the analyzed pixel. The technique was applied to an aluminum plate, whose results showed high probability values near the damage's location.

Zhu *et al.* [11] used a combination of the direct coupling mechanical impedance (DCMI) methodology for signatures extraction and a modified probability-weighted function to locate damage in a honeycomb sandwich composite plate. After defining the optimal sensing radius of

the PZT patch, the raw signatures were processed using the DCMI methodology and used to calculate RMSD indexes. The probability-weighted algorithm could delineate the damage's position once the higher probabilities were located near the real location of the damage, especially in the results obtained from the DCMI signatures.

The prediction of damage in a honeycomb sandwich composite plate was explored also in Sikdar *et al.* [12]. Since conductance signatures are affected by PZT patches-debonding distance, a debond index was formulated, reasoned by the differences in the experimental and numerical conductance signatures. Maps of debonding's probability were generated from the proposed index, whose results showed good compatibility between estimated and real damage's position.

Based on the spatial correlation among damage metric values in the sensor grid, Gonçalves *et al.* [13] used the ordinary kriging (OK) method to estimate the location of damage in aluminum plates. Four damage scenarios were considered. From the spatial information obtained by semivariogram, the RMSD values were interpolated by OK, resulting in maps of RMSD values, in which the higher ones were located at the respective damage positions.

The spatial correlation between damage metric values was also explored by Gonçalves *et al.* [14]. The indicator kriging (IK) technique was used to estimate the damage's probability of occurrence. It considered five scenarios of sensor grids with different spacing. The probability maps showed higher values located at the plate's center, where the damage was positioned, being possible to delineate the region of failure by the proposed approach.

Still, based on the relationship between damage metrics and distance from the damage, Soman *et al.* [15] proposed an inverse implementation to preview the damage location in a glass fiber-reinforced polymer (GFRP) plate. An analytical model was formulated, relating the damage metric and the PZT patch-damage distance and relative angle, resulting in a dataset of damage index. The experimental indexes were compared with the numerical ones, and the scenario with the lowest mean absolute error (MAE) was defined as a representative to determine the damage position. The results showed the method's ability to estimate the damage's location.

Wang *et al.* [16] proposed the use of three frequency intervals, based on finite element model (FEM) results, to detect and locate a loosened bolt. The information collected was used in a Support Vector Machine (SVM), resulting in a recognition accuracy of 81.25%, whereas using a single interval resulted in a maximum accuracy of 65.5%.

Based on a FEM model of an aluminum beam, Fan and Li [17] compared the sparse and Tikhonov regularization methods for damage location. The FEM was adjusted, and the frequency shifts of the Conductance spectra's resonance peaks were used in the regularization methods to solve the inverse problem. The change in Young's modulus was used as the damage index. The sparse regularization could estimate the damage position in all scenarios considered, unlike the Tikhonov regularization, which estimated the real position in just a few scenarios.

Even with this, the existing methods have limitations in that they solely focus on estimating the damage's location without offering insights into the reliability of the data collected from the sensor grids, even in cases following the OK approach. Therefore, understanding the spatial uncertainty associated with a sensor grid becomes imperative in designing an optimal sensor arrangement.

Here, the concept of a sensor grid is related to data, computing, information, and knowledge discovery management. In contrast, the sensor network concept is attributed to sensors' logical and physical connectivity [18].

This contribution presents an innovative approach rooted in Sequential Gaussian Simulation (SGS). Its main objective is twofold: firstly, to estimate the location of known damage and, secondly, to quantify the spatial uncertainty of the Root Mean Square Deviation (RMSD) indices through an aluminum plate. This approach opens new perspectives for optimizing sensor grid designs by offering a detailed uncertainty map. Furthermore, the impact of sensor spacing on

spatial uncertainty is the subject of studies, where regular and non-regular sensor grids with varying spacing are meticulously evaluated. Finally, the effectiveness of the SGS approach in accurately estimating damage positions is subject to rigorous evaluation.

2. Theoretical backgrounds

This section presents concepts related to the techniques and tools used in this work. It includes explanations of the Electromechanical Impedance method, Geostatistics, and the SGS method.

2.1. *Electromechanical impedance*

The Electromechanical Impedance (EMI) technique is based on the electromechanical coupling between the monitored structure and a piezoelectric element, usually a PZT patch, attached to it. Due to this interaction, the electrical impedance measured in the PZT patch's terminals is related to the mechanical impedance of the hosted structure, being a signature of its state [1, 19, 20].

The PZT patch-structure can be considered as a spring-mass-damper system of 1 degree of freedom, whose formulation was presented by Liang *et al.* [21]. In this system, the PZT patch is excited by a harmonic voltage signal resulting in an induced strain, affecting locally the structure. Then, the dynamic response of this one is transferred back to the sensor, represented by an electrical signal [19, 22].

The relation between the electrical impedance ($Z_E(\omega)$) and the structure's mechanical impedance ($Z_s(\omega)$) can be described by the mathematical model given by Equation (1) [21], which varies along a frequency (ω) interval. In Equation (1), τ is the geometric constant of the PZT patch; j, the imaginary unit; ε_{33}^{T}, the dielectric constant for a given mechanical stress T; Z_p is the transducer's mechanical impedance; d_{3X}^2, the dielectric constant, and; Y_{XX}^E, the Young's modulus for a constant electric field E.

$$Z_E(\omega) = \frac{1}{\mathrm{j}\omega\tau}\left(\varepsilon_{33}^{T} - \frac{Z_s(\omega)}{Z_s(\omega)+Z_p(\omega)} d_{3X}^2 Y_{XX}^E\right)^{-1}. \tag{1}$$

The application of an AC voltage signal to the PZT patch with a frequency interval provides a signature of the electrical impedance, which indicates the structural conditions due to the electromechanical coupling. Thus, any changes in the impedance signatures can indicate structural integrity changes [20, 23].

Comparing the impedance signatures, usually their real parts (Resistance), at any moment with those of the pristine state (baseline signature) allows the detection of damages. Based on this, damage indexes were developed to indicate it quantitatively. Among them, the most used is the Root Mean Square Deviation (RMSD), defined in Equation (2), and based on a Euclidean norm [1, 24].

$$\mathrm{RMSD} = \sqrt{\frac{\sum_{k=\omega_i}^{\omega_f}[Z_E(k) - Z_E^0(k)]^2}{\sum_{k=\omega_i}^{\omega_f}[Z_E^0(k)]^2}}. \tag{2}$$

The RMSD index quantifies the changes in two signatures by calculating the square root of the mean quadratic differences between the kth electrical impedances at a particular moment ($Z_E(k)$) and at the pristine condition ($Z_E^0(k)$), along a frequency interval defined by its lower (ω_i) and upper (ω_f) limits.

The quantification of damage metrics for a sensor grid provides crucial information for damage assessment, allowing better decision-making regarding structure maintenance.

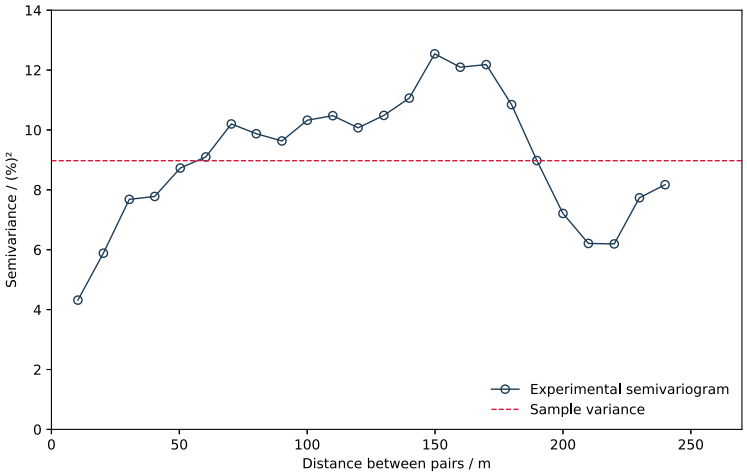

Figure 1. Example of an experimental semivariogram.

2.2. *On concepts of geostatistics*

Geostatistics had its roots as an application of Georges Matheron's Theory of Regionalized Variables [25–28] and was first developed to address geological and mining engineering problems, and is widely used in these fields [29–32]. By gathering a finite number of samples, geostatistical methods are employed to create geological models by interpolating the sample values. The interpolation is based on analyzing the distribution and correlation of the sample values within the study area.

The type of variables treated by geostatistical techniques exhibit spatial continuity within the studied area. This continuity results in data points close to each other having similar values, leading to reduced dissimilarities among them. Conversely, data points that are distant from each other exhibit a higher contrast between the corresponding values [33].

This behavior implies that not only the variable's values are used in the analysis but also their relative positions. To quantify the spatial continuity, it is used the semivariogram function (Equation (3)), which calculates half of the mean squared differences between two values ($z(x_i)$ and $z(x_i + h)$) separated by a vector h [34, 35].

$$\gamma(h) = \frac{1}{2N(h)} \sum_{i=1}^{N(h)} [z(x_i) - z(x_i + h)]^2. \tag{3}$$

The calculation of the semivariogram for several classes of the distances h provides a quantification of the spatial continuity along the direction under examination. Comparing the semivariogram values and corresponding distances yields an experimental semivariogram (Figure 1), demonstrating a steadily increasing trend that denotes a decrease in continuity with increasing separation distance between pairs of sample data [36].

For use in the estimation or simulation processes, it is necessary to fit the experimental semivariogram with theoretical functions, once the calculated semivariogram is a discrete function with no semivariance values between two successive distance classes. Spherical, exponential, and Gaussian mathematical models (Figure 2a) are commonly employed to fit the computed semivariogram [36].

A typical semivariogram model has three parameters (Figure 2b) that define its shape: Nugget Effect, Range, and Sill. The Nugget Effect represents a discontinuity at the origin of the semivariogram and indicates spatial variability occurring at a significantly smaller scale than the

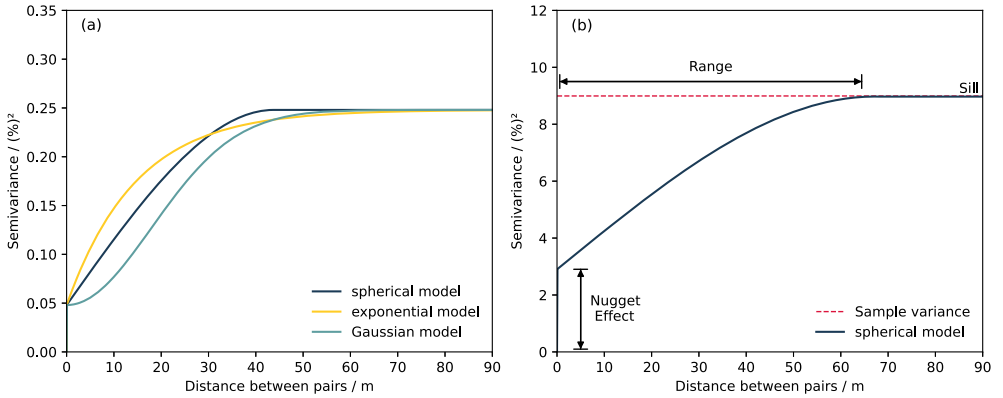

Figure 2. Some theoretical models for semivariogram fitting (a) and semivariogram model with its properties (b).

data spacing. The Range refers to the distance beyond which no spatial correlation exists between sample pairs, while the Sill corresponds to the data variance along the vector's h direction [37].

The semivariogram model derived from fitting is utilized in various geostatistical-based estimation and simulation techniques, such as the SGS method.

2.3. *Sequential Gaussian simulation*

The SGS is a stochastic simulation method characterized to have a sequential nature, once the simulation of a given point in the space is based on the sampled and previously simulated values within the search neighborhood [35, 36].

The original random function (RF), which comprises a vector of the sampled values at the analyzed domain, is transformed into a standard normal distribution before the implementation of the SGS algorithm [33]. The use of another distribution, despite honoring the mean, variance, and semivariograms (for fundamental concepts, refer to Armstrong [38], Isaaks and Srivastava [39], and Journel and Huijbregts [34]), results in the incorrect global distribution of simulated values, which is not a problem in a Gaussian space [37].

The generation of a simulated value $Y^*_{\mathrm{SGS}}(u)$ at a given node u is done initially by estimating a value $Y^*_{\mathrm{SK}}(u)$ by simple kriging (SK) method (Equation (4)) using the sampled and previously simulated data at the u_β locations, which have, each one, a weight resulted from the solution of the SK system [37, 40]. Once the Gaussian mean (m) is zero, the second term of the Equation (4) is zero, keeping only the first one.

$$Y^*_{\mathrm{SK}} = \sum_{\beta=1}^{n} \lambda_\beta Y(u_\beta) + m\left(1 - \sum_{\beta=1}^{n} \lambda_\beta\right). \tag{4}$$

From SK it's obtained an estimated value $Y^*_{\mathrm{SK}}(u)$ at a given node u and its associated kriging variance ($\sigma^2_{\mathrm{SK}}(u)$), that are used for selecting a random residual ($R(u)$) from the Monte Carlo simulation that yields a normal distribution with null mean and variance equal to the SK variance. The residual is then, added to the SK estimate (Equation (5)), resulting in the simulated value [33, 37, 41].

$$Y^*_{\mathrm{SGS}}(u) = Y^*_{\mathrm{SK}}(u) + R(u). \tag{5}$$

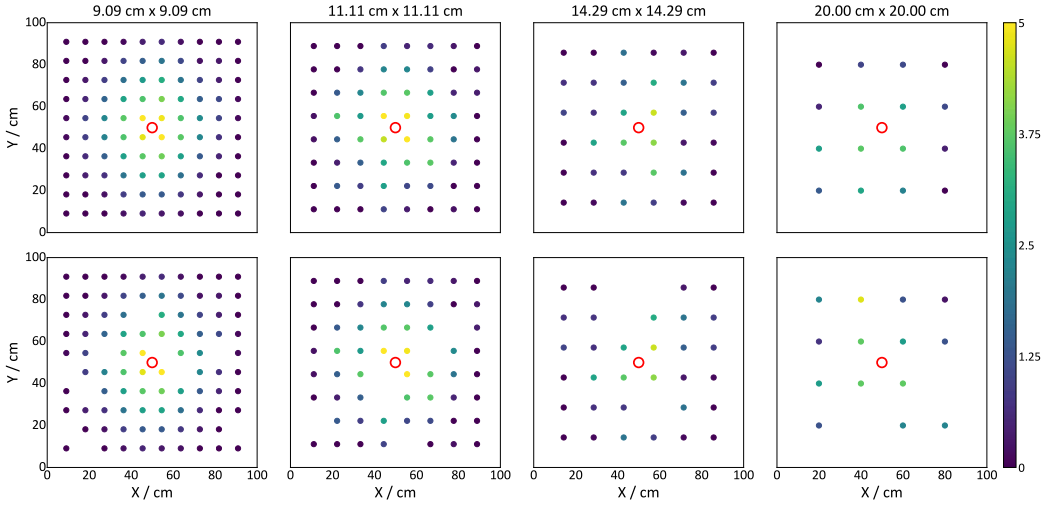

Figure 3. Maps depicting the positions of sensors under regular grid conditions (first row) and non-regular grid conditions (second row). The red circle designates the location of the actual damage.

The simulated value is added to the conditioning data to ensure that the covariance between all of the simulated values is reproduced, thus, providing reproducibility of the input statistical distribution and the covariance models, unlike the Kriging results, which is smoothed [42].

This process is repeated along the domain randomly to avoid artifacts, and each node is visited only once, preserving those in the sampled locations [41], resulting in conditional-to-data simulations. Once a different seed is used for each realization, providing different simulation paths, it results in equiprobable scenarios, which can be used for spatial uncertainty analysis.

3. Materials and methods

The spatial uncertainty of damage metric values was initially evaluated using four regular grids, whose data sets were obtained from Gonçalves *et al.* [14]. In this context, it was considered the following spacings between sensors in the regular grids: (1) 9.09 cm × 9.09 cm (10 × 10 PZTs); (2) 11.11 cm × 11.11 cm (8 × 8 PZTs); (3) 14.29 cm × 14.29 cm (6 × 6 PZTs), and; (4) 20.00 cm × 20.00 cm (4 × 4 PZTs), all of them showed in Figure 3.

Based on the primary regular grids, the results derived from the SGS approach were also analyzed under non-regular grid conditions. In each sensor grid scenario, 10.0% of the total information was randomly removed, resulting in areas within the grid with no recorded data, as shown in Figure 3.

In all scenarios of sensor spacing, the damage of the same severity was simulated in the center of the square aluminum plate of 100 cm × 100 cm dimensions. In these cases, simulated damage was done by adding mass corresponding to an M6 nut (3.1 g) glued to the center of the plate. The procedures and tools used were consistent across all conditions and are detailed below, with the corresponding flowchart shown in Figure 4.

Once the SGS algorithm need the data to be transformed into a Gaussian distribution, the original input data was first transformed to a standard Gaussian distribution, which was done by using the *nscore* module of the Pygeostat package for Python [43]. The Gaussian transformed data was submitted to structural analysis by semivariograms with the aim of identifying the

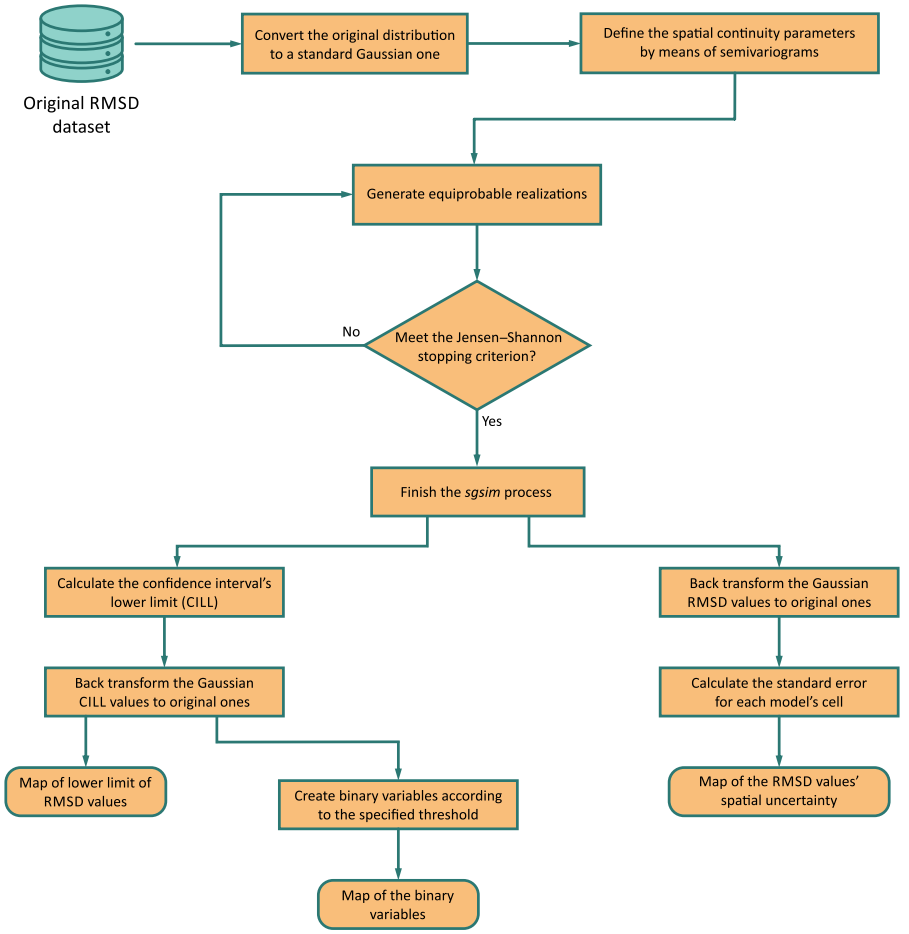

Figure 4. Flowchart of the executed steps.

preferential directions of continuity. The calculation and theoretical fitting of the semivariograms were done using the GeostatsPy Python Package [44].

The resulting semivariogram fitting was the basis for generating the equiprobable realizations by SGS, executed in the *sgsim* algorithm adapted to Python language in the Pygeostat package [43]. The generated realizations were conditional, as the simulated values at the nodes with input data were equal to these, to reproduce the variable's spatial continuity more properly.

The parameters used in the *sgsim* algorithm were the following: (1) file with data; (2) number of the columns containing the X and Y coordinates and the variable to be simulated; (3) range of the data to be considered in the simulations; (4) the lower and upper limits of the Gaussian distribution obtained by the *nscore* process; (5) random seed; (6) parameters of the grid-like model used to store the realizations; (7) number of realizations to be generated; (8) the minimum and maximum sample data and simulated nodes employed in each simulation; (9) semivariogram fitting outcomes; (10) search ellipsoid parameters, and; (11) type of kriging to be used.

The input file comprised X and Y coordinates of each PZT patch in the first and second columns, respectively, and normal score-transformed RMSD values in the last column. The utilized format adhered to GeoEAS standards, as required by the *sgsim* process.

For the simulations, all the normal score-transformed RMSD values were considered to fully

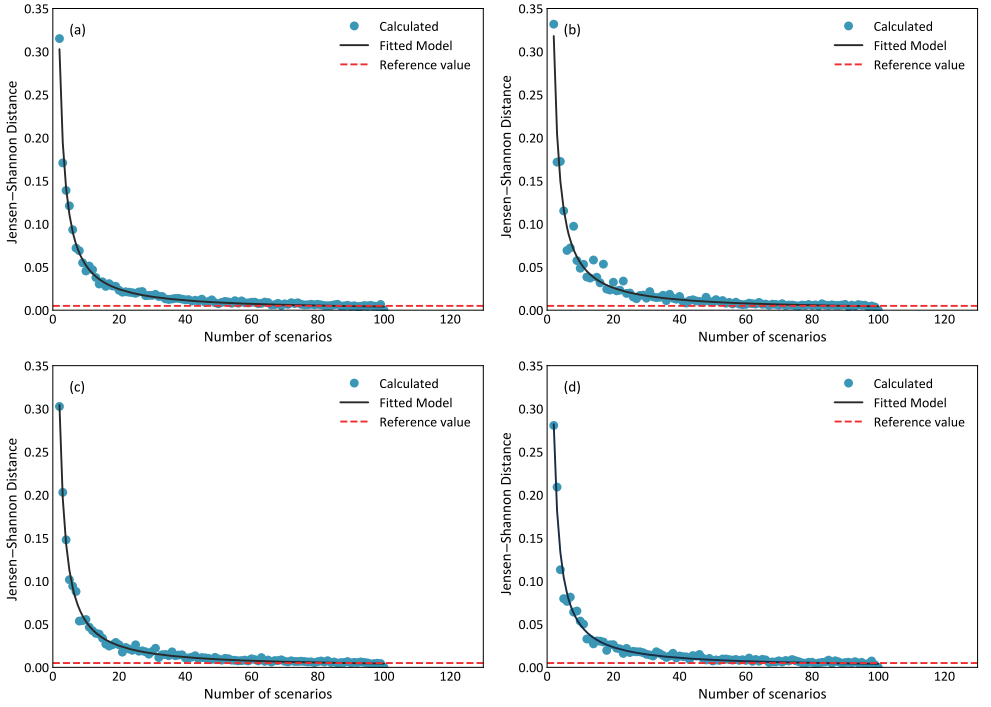

Figure 5. Calculated Jensen–Shannon values and theoretical fitting for the 9.09 cm × 9.09 cm (a), 11.11 cm × 11.11 cm (b), 14.29 cm × 14.29 cm (c), and 20.00 cm × 20.00 cm (d) sensor spacing grids.

map the entire structure instead of focusing on specific values.

The random seed is the first value initializing the simulations and corresponds to a large odd integer. To ensure unbiased results, a seed was chosen from a random process for each simulation.

To store the realizations, a model consisting of unit cells with dimensions of 4.00 cm × 4.00 cm was utilized, resulting in a resolution of 4.00 cm. The dimensions of the specified cell were chosen due to the following: (1) being smaller than all semivariogram ranges; (2) being a multiple of the plate's size, contributing to aligning the model with the plate's dimensions, and (3) being smaller than the sensor spacing in all scenarios evaluated.

The number of cells in each direction was determined by dividing the plate size along the given axis by the corresponding unit cell dimension, resulting in a grid-like model with the same dimensions as the monitored structure.

The number of realizations adopted was 91. This value was the highest number of realizations among all sensor grid scenarios at which the variance of the RMSD values stabilizes. The stabilization criteria were the value of 0.005 of the Jensen–Shannon distance calculated between the variance's statistical distribution of two sequential numbers of realizations. Figure 5 shows the Jensen–Shannon calculated values and their respective theoretical fitting; the latter determines the realization number at which the variance stabilizes.

The minimum and maximum sample data for the simulations were set as 1 and 6, respectively. This selection ensures that the search neighborhood includes at least one PZT patch for node simulation and no more than 6 PZT patches to reduce the impact of distant data that may affect the local estimation. In addition, the number of simulated nodes used for a given node was set to 5 to further reduce the influence of distant data on the local estimation. The chosen values were

utilized to simulate all scenarios to provide a comparative analysis.

Once the semivariogram is a quantitative description of the spatial continuity of the variable being simulated, the dimensions and orientations of the search ellipsoid were set equal to the corresponding range and directions of the semivariograms.

As stated in the section outlining the SGS methodology, the SK method was the fundamental estimator in all simulations.

The realizations obtained for all scenarios had Gaussian distribution, reproducing the histogram and spatial continuity of the respective input data. Once each cell in the model had a standard normal distribution of simulated RMSD values, it was calculated the lower limit of the confidence interval (CI) for a significance level of 5.0%, which was converted to original values through the Pygeostat package's *backtr* process [43].

The lower limit of the CI was used to ensure that the lowest possible values for the mean, for the considered significance level, would be used in the later steps.

To visualize only the region of the damage location, a threshold equal to the 95th percentile was selected, as seen in Soman *et al.* [15]. In this way, each scenario had its specific threshold, according to the RMSD sample data. From the selected threshold, binary variables were created for the values of the confidence interval's lower limit, according to Equation (6) so that the ones indicate RMSD values higher than the specified threshold.

$$I_{95}(x) = \begin{cases} 1, & \text{if RMSD}(x) > t_{95} \\ 0, & \text{otherwise.} \end{cases} \tag{6}$$

In the Equation (6), $I_{95}(x)$ corresponds to the indicator variable at a location x; RMSD(x), the lower limit for the RMSD values at a location x, and; t_{95}, the specified threshold. The resulting maps were used to analyze the ability of the approach to delineate the damage's position in each scenario.

Based on the indicator maps, which delineate the regions of possible damage occurrence, the centroids of the areas with $I_{95}(x)$ equal to 1 were calculated, estimating the damage position. For this purpose, the spatial coordinates of the binary values were obtained by means of the Pygeostat package's *addcoord* module [43], once these had no coordinate attributed to them. The centroids obtained were compared to the actual damage position in each scenario of sensor spacing using the Euclidean distance as the parameter.

In all scenarios, the RMSD spatial uncertainty $U(x)$ at each location x was calculated as the standard error (Equation (7)) of the 91 simulated values in each cell's model since each cell contains a statistical distribution of RMSD indexes. For its calculation (Equation (7)), the standard deviation $s(x)$ was previously defined at each location x, considering the number of realizations (n).

$$U(x) = \frac{s(x)}{\sqrt{n}}. \tag{7}$$

The nature of the standard error, as this parameter provides a normalized value associated with data variability, allows the mapping of areas with high variability, which provides several possibilities in the design of sensor grids.

4. Results and discussions

The maps in Figure 6, which depict the confidence interval's lower limit of the simulated RMSD values, show a gradual change in values from high values near the center of the plate to low ones at the borders, away from the damage, under both regular and non-regular grid conditions. As the spacing between sensors increases, the RMSD values become smaller, which is expected.

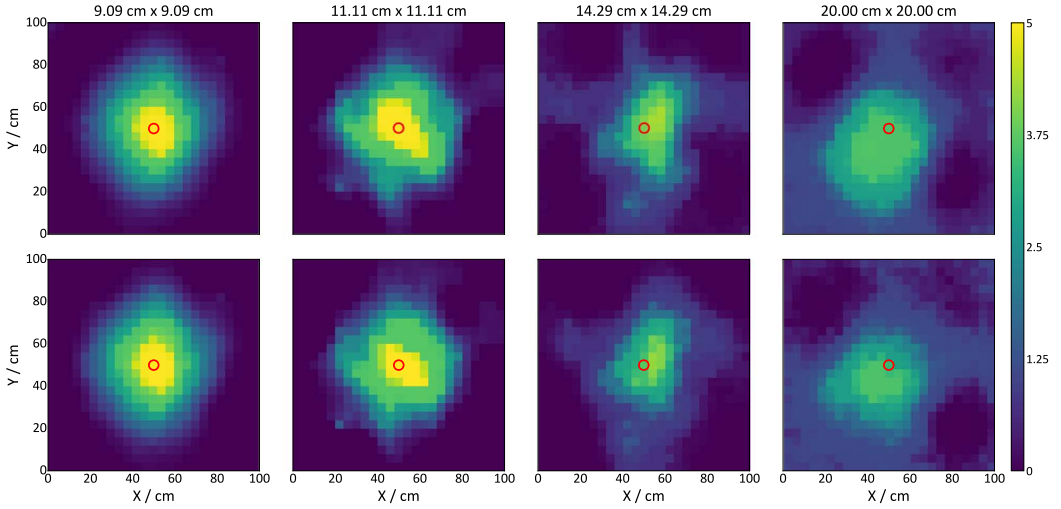

Figure 6. Maps showing the lower confidence interval limit of simulated RMSD values by SGS under regular (first row) and non-regular (second row) grid conditions. A red circle indicates the location of the actual damage.

Additionally, the area with relatively high index values increases, as seen in the scenario with a spacing of 20.00 cm × 20.00 cm.

The resulting maps indicate that the random removal of PZT patches resulted in noticeable changes in scenarios with fewer samples (14.29 cm × 14.29 cm and 20.00 cm × 20.00 cm). However, PZT patch removal had a smaller impact in scenarios with more data, which was anticipated due to the higher information available.

However, in all scenarios, it is possible to identify the presence of damage near the plate's center, as the highest values of RMSD are in this region, which makes the proposed approach capable of mapping the area with the occurrence of damage, even in the scenario with a little amount of information (4 × 4 PZT patches).

The results obtained with the SGS method (Figure 6) represent the sample data spatially, meaning that regions with low sample values had lower simulated values and vice versa. This behavior has been observed in other works that have employed SGS [45–50], where the simulated values follow the spatial variability of the sample values.

The variation of simulated RMSD values along the plate based on the spatial distribution of sample data supports the potential use of the method in other scenarios, including those where damage is located at the border of the plate. In this regard, Gonçalves, Moura Junior and Pereira [13] utilized Ordinary Kriging (OK), an alternative geostatistical approach, to interpolate RMSD values on a square plate with border damage, resulting in favorable outcomes.

In spite of this fact, this topic is outside the scope of this study, which intends to introduce potential applications of the SGS method in developing sensor grids for SHM. Subsequent research studies could examine supplementary damage scenarios, encompassing multi-damage situations, to evaluate the efficacy of the SGS method in detecting structural damage.

Figure 7 displays the lower limit values higher than the 95th percentile as green areas. The binary values were calculated utilizing Equation (6) to delineate regions of damage occurrence. According to the first two scenarios (10 × 10 and 8 × 8 PZT patches) under regular and non-regular grid conditions, the green area encompasses the center of the plate, allowing the damage location to be confidently delineated.

In contrast, the green area predominantly covers the center of the plate in the regular grid

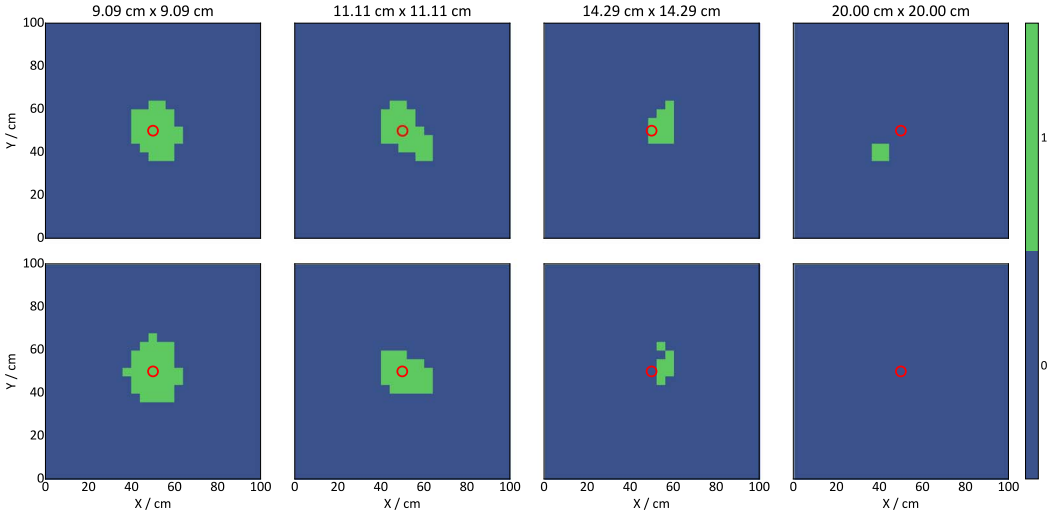

Figure 7. Maps showing binary variables associated with the threshold applied to the lower limit of confidence intervals for simulated RMSD data for the regular (first row) and non-regular (second row) data sets. The location of the actual damage is marked with a red circle.

condition with 6 × 6 PZT patches, whereas the non-regular grid condition does not include the plate's center. For the 4 × 4 PZT patches scenario with a regular grid, the green area does not cover the plate's center, and the non-regular grid condition fails to highlight an estimation of the damage location.

Also, Figure 7 indicates that the predicted area of damage shifts away from the center of the plate as the spacing between the PZT patches increases, which can also be seen in Figure 8, where the damage's estimated location (purple circles), referred to as the centroids of the green areas in Figure 7, becomes more distant from the plate's center (red circles) as the sensor spacing widens.

Additionally, while it may be challenging to compare non-uniform conditions once samples were removed randomly in each scenario, Figure 8 reveals a general trend of increased deviation between predicted and actual locations as sensor spacing increased.

Also, the findings indicate that, typically, the distances from the actual damage location tended to increase within the same spacing when eliminating PZT patches, and the damage location could not be estimated for the 4 × 4 PZT patches scenario with non-regular grid conditions.

The findings above are detailed in Figure 9a, which displays the Euclidean distance between the estimated and actual damage locations. As per the outcomes, the highest distance from the actual damage, within the regular grid condition, was 14.14 cm, attributed to the 20 cm × 20 cm sensor spacing, which represents an increase of 1350% about the lowest one (0.98 cm), attributed to the 9.09 cm × 0.09 cm spacing.

Figure 9a indicates a general distance increase as the sensor spacing widens in the non-regular grid condition. There is also an increase in distance within the same spacing category about the regular grid status. This effectively summarizes the findings drawn from the maps mentioned previously (Figures 7 and 8).

The 9.09 cm × 9.09 cm spacing scenario was an exception to this overall behavior. In this one, removing samples reduced the distance from the actual damage, with a 15.6% reduction being detected. It is possible that the random removal of some specific samples contributed to this slight improvement in results, as the SGS method relies on the special continuity among sampled

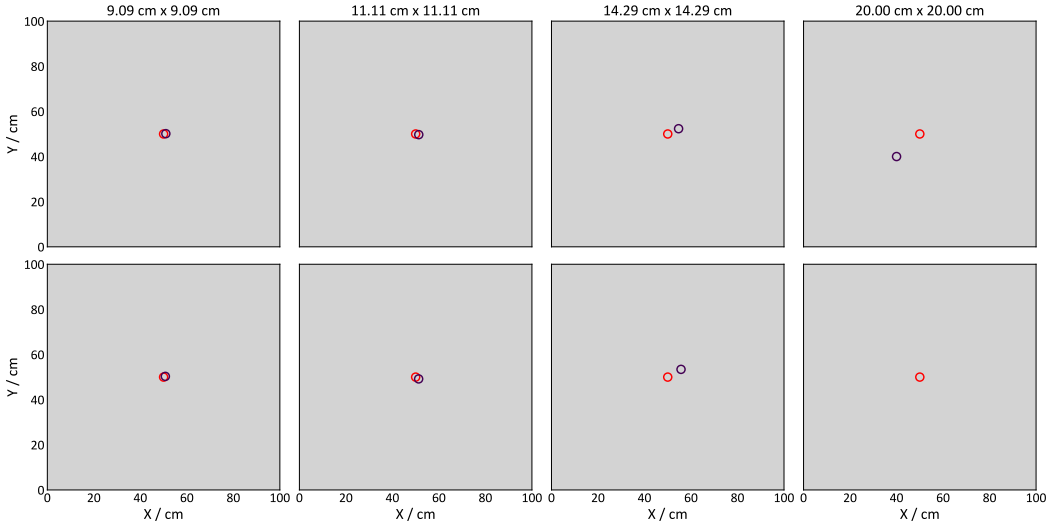

Figure 8. Maps showing the actual location of the damage (red circle) and the estimated location (purple circle) calculated using the corresponding centroids on both uniform grid (first row) and non-uniform grid (second row) conditions.

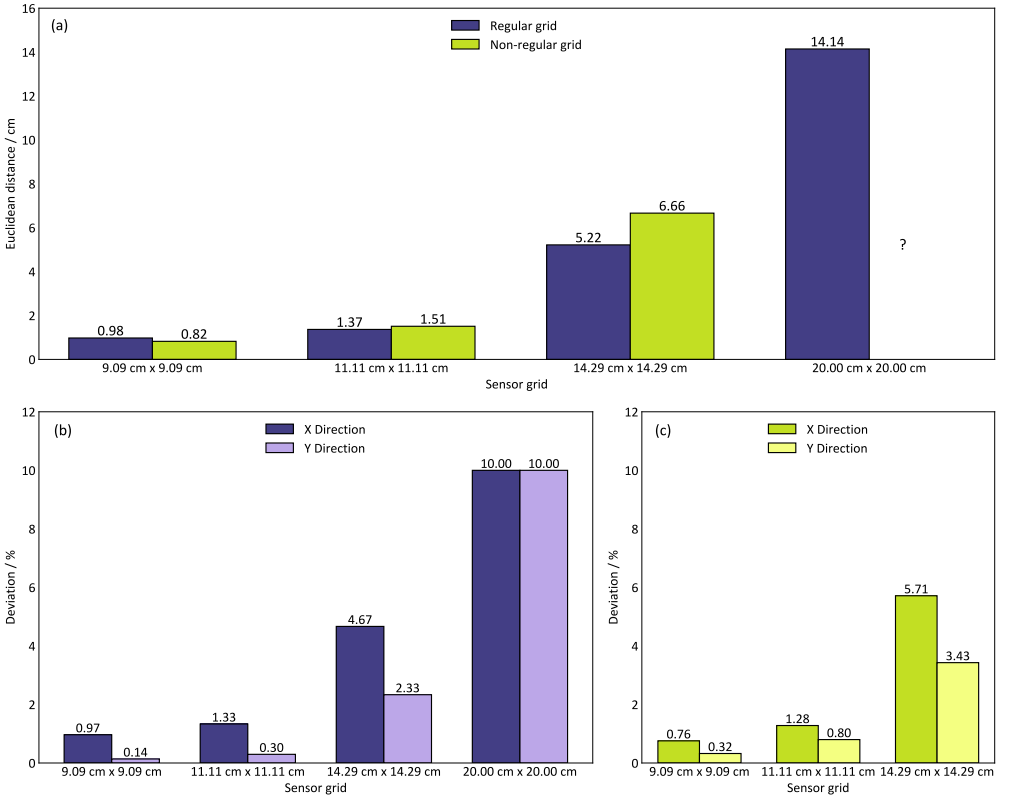

Figure 9. Distance between the estimated and actual damage positions (a) and percentage of the distance between estimated and actual positions about each plate's dimension for both regular grid (b) and non-regular grid (c) conditions.

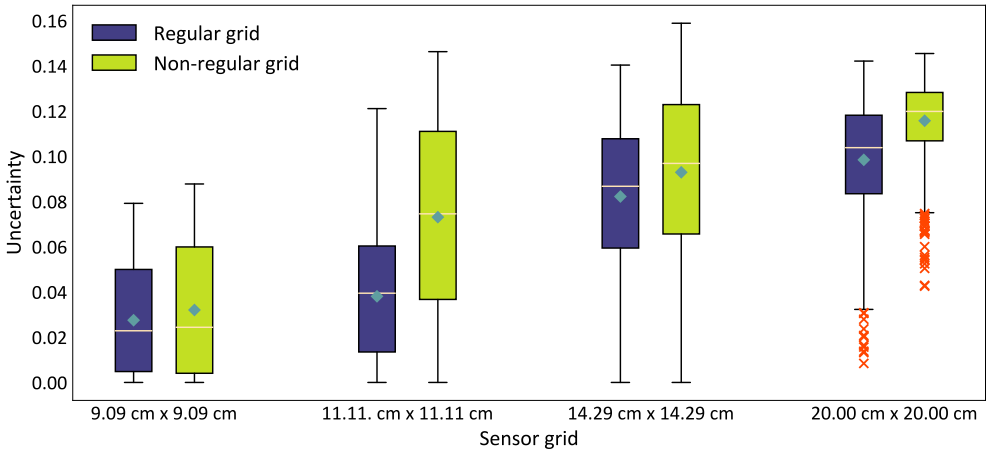

Figure 10. Boxplots of the standard error for each sensor spacing and grid type.

points to provide the estimations.

Furthermore, the scenario that exhibited the most significant increase in distance after removing samples was the 14.29 cm × 14.29 cm spacing, whereby the distance was augmented by 27.7%. This suggests that scenarios with fewer samples could be more sensitive to reduced available information. However, new research is needed to investigate this issue.

Despite the highest distance between the estimated and real damage's location being relatively high in value (14.14 cm), the decomposition of the distances along X and Y directions reveals that even in the scenario with the most increased sensor spacing in the regular grid condition, the distance along X and Y represents only 10.0% of the respective plate's dimensions (Figure 9b).

Considering the non-regular grid status (Figure 9c), the deviation from the plate's dimensions in both directions was similar to that obtained with a regular grid configuration. However, determining the damage location for a 20.00 cm × 20.00 cm spacing with a non-regular grid was not feasible.

The results demonstrate that utilizing a consistent layout of sensors allows for reasonable estimation of the damage location, even when operating with the maximum spacing scenario considered (20.00 cm × 20.00 cm spacing). Conversely, non-regular grid arrangements face limitations when processing sparse data. Nonetheless, after randomly eliminating PZT patch data, further research is required to explore these issues in greater detail.

The absence of an estimation regarding the location of damage in the 4 × 4 PZT patches with a non-uniform grid, using the lower bound of the confidence interval, can be ascribed to an extended range of confidence intervals. This extension may have been caused by removing samples that elevated variance among realizations.

The increasing trend in variance among realizations as the spacing between sensors increases and samples are removed can be seen in Figure 10, which depicts the statistical distributions of the standard error among realizations.

Once the variance, and then the standard deviation, is related to the standard error using Equation (7), these are correlated so that the variance has the same behavior as the standard error.

Considering the regular grid condition, the findings show that the standard error parameter increases as the sensor spacing widens. In the scenario with the smallest spacing (9.09 cm × 9.09 cm), the mean and maximum standard error values are 0.0275 and 0.0792, respectively. As the sensor spacing increases from 9.09 cm × 9.09 cm to 11.11 cm × 11.11 cm, there is a 38.4% increase in the mean and a 52.9% increase in the maximum value. The differences in

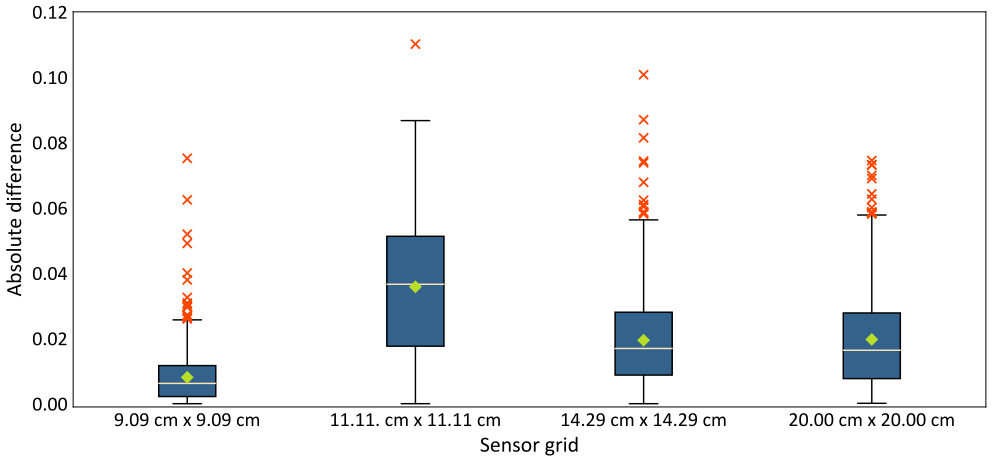

Figure 11. Boxplots of the absolute difference in the standard error between the regular and non-regular grid conditions.

mean and maximum values are even greater when compared to the 14.29 cm × 14.29 cm sensor spacing, with mean and maximum values being 198.7% and 77.2% higher than the respective ones in the 9.09 cm × 9.09 cm spacing. In the highest spacing scenario (20.00 cm × 20.00 cm), the minimum standard error value was not zero, and lower values were classified as outliers, unlike other scenarios.

Figure 10 shows that removing samples increased the uncertainty parameters for each category of sensor spacing. However, since the sample removal was random in each scenario, comparing consecutive sensor spacing scenarios is difficult. Despite this limitation, there is an overall increasing trend as the sensor spacing widens, as observed in the regular grid condition.

When comparing the average uncertainty parameter between the non-regular and regular grid states, it is evident that the 11.11 cm × 11.11 cm spacing scenario was most affected by the sample removal, as the average standard error increased by 91.9%. Since the samples were removed randomly, removing a particular group of samples could have caused this behavior. In the other scenarios, the average uncertainty increased by a similar magnitude.

The absolute difference in the standard error results between the irregular and regular grid conditions (Figure 11) shows that the highest differences were also attributed to the 11.11 cm × 11.11 cm spacing, whereas the 9.09 cm × 9.09 cm spacing was the less affected scenario, likely due to the higher available information in the 9.09 cm × 9.09 cm sensor spacing.

Once samples have been removed randomly, it becomes difficult to compare different spacing scenarios. However, a preliminary analysis indicates that removing samples generally does not significantly affect conditions with a higher number of sensors. However, reducing the number of sensors has a more significant impact on systems with limited information. This aspect must be investigated in detail in future research.

The mapping of the spatial distribution of the absolute difference between the standard errors of the non-regular and regular grid conditions (Figure 12) shows an overall increase in the uncertainty parameter near the sites where the samples were previously located. This suggests that removing PZT patches increases the spatial uncertainty of the damage index values in their vicinity.

The uncertainty map in Figure 13 displays an increase in parameter uncertainty for the regular grid condition as the sensor spacing widens, resulting in the greatest standard error values in the scenario with a 20.00 cm × 20.00 cm spacing. Additionally, removing samples within the same spacing category increased the uncertainty, as discussed previously.

Figure 13 also highlights ring-shaped areas with higher uncertainty values for a given sensor

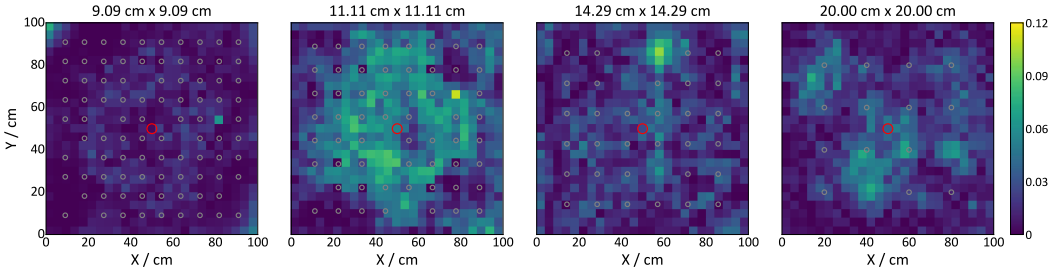

Figure 12. Maps showing the absolute difference in standard error before and after sample removal across the plate. A red circle indicates the location of the damage, while the gray circles represent the positions of the PZT patches.

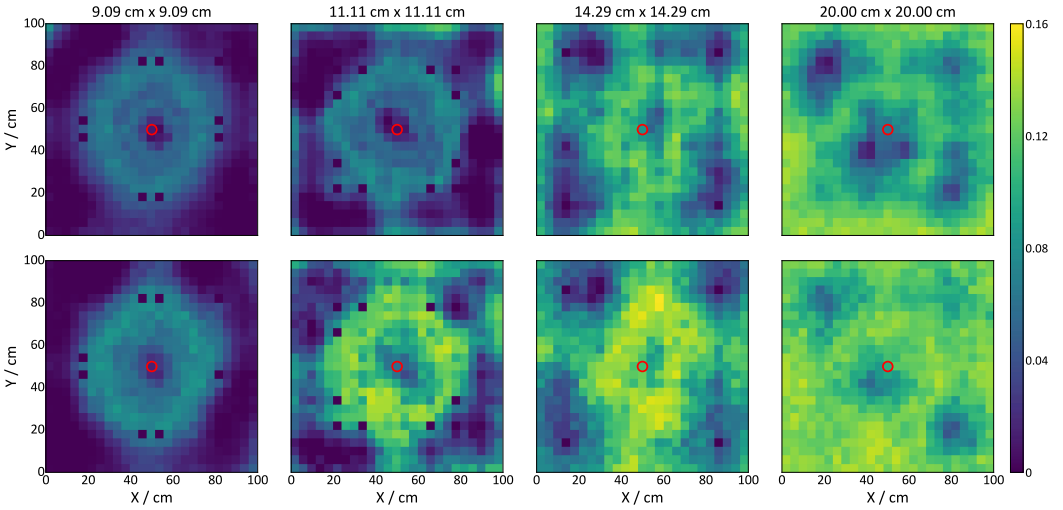

Figure 13. Maps showing the standard error results for both regular (first row) and non-regular (second row) data sets. The location of the actual damage is marked with a red circle.

spacing, indicating a high spatial variation of RMSD indexes in those regions. This may suggest a transition zone from low to high RMSD values. Conversely, low uncertainty values in certain areas suggest low spatial variability of the damage metric, indicating stable RMSD data in those regions.

The behavior described above is most evident when using a 9.09 cm × 9.09 cm and a 11.11 cm × 11.11 cm sensor spacings. Standard error values are also low near the edges of the plate, where damage metric values are uniformly low (as shown in Figure 3). However, as the RMSD values gradually increase from the edges to the center of the plate, spatial variability in the damage metric values becomes more pronounced, leading to higher standard error results.

According to the findings, the uncertainty maps help identify areas with high spatial variability in the damage indexes. Based on the spatial uncertainty results, it may be inferred that there is a lack of sensor information in these regions, making it challenging to locate damage accurately.

Alternatively, the spatial uncertainty results may be used to quantify the level of uncertainty associated with a sensor grid. Therefore, the results obtained from the SGS approach can be a valuable tool for designing sensor grids that consider uncertainty.

5. Conclusions

This study discusses the effectiveness of the SGS method in identifying damaged positions within an aluminum plate. The investigation involved analyzing four regular sensor grids with varying sensor spacings. Additionally, the effect of sample removal was investigated for each scenario of sensor spacing by randomly removing samples.

The results indicate that the method demonstrated proficiency in estimating damage locations for the regular grid condition, with the minimum and maximum distances between estimated and actual damage being recorded at 0.98 cm and 14.14 cm, respectively. These measurements correspond to the narrowest and widest sensor grids examined in the study.

Removing samples increases the deviations from the actual damage location in each scenario. Additionally, under the non-regular grid conditions, predicting the damage location in the 20.00 cm × 20.00 cm spacing scenario was impossible using the lower limit of the confidence interval approach.

This absence of damage prediction for the non-regular-based 20.00 cm × 20.00 cm sensor spacing may be due to increased variance among realizations. This was confirmed by analyzing the standard error distribution in each condition, which showed an overall increase with sample removal for the same spacing class. Also, this increasing trend was most evident near the position of the removed samples.

Additionally, the mapping of the standard error shows an overall increase in uncertainty as the sensor spacing widens. This provides insight into the reliability of a sensor grid quantitatively.

Using the SGS method to map the spatial uncertainty of the damage index along the structure provides valuable information for designing sensor grids that consider this parameter. This information can be used to identify areas that require careful treatment, offering new insights into the design of sensor grids.

The SGS method applied to the ISHM can provide several possibilities. Future research can be focused on (1) determining an optimal sensor arrangement based on uncertainty information, (2) investigating the capacity of the method to predict multiple damage positions, and (3) evaluating the industrial application of the proposed approach.

Declaration of interests

The authors do not work for, advise, own shares in, or receive funds from any organization that could benefit from this article, and have declared no affiliations other than their research organizations.

Dedication

The manuscript was written through contributions of all authors. All authors have given approval to the final version of the manuscript.

Acknowledgments

The first author is grateful to the Federal University of Catalão in provinding license to study doctorate at the Federal University of Uberlândia.

References

[1] V. Giurgiutiu, *Structural Health Monitoring with Piezoelectric Wafer Active Sensors*, 2nd ed., Academic Press, Waltham, 2014.

[2] A. N. Zagrai, V. Giurgiutiu, "Electromechanical impedance modeling", in *Encyclopedia of Structural Health Monitoring* (C. Boller, F.-K. Chang, Y. Fujino, eds.), John Wiley & Sons, Chichester, 2009, p. 5.

[3] Q. S. S. Nomelini, J. W. Silva, C. A. Gallo, R. M. Finzi Neto, K. M. Tsuruta, J. R. V. Moura Jr, "Non-parametric inference applied to damage detection in the electromechanical impedance-based health monitoring", *Int. J. Adv. Eng. Res. Sci.* **7** (2020), no. 9, p. 73-79.

[4] I. I. C. Maruo, G. F. Giachero, V. Steffen Jr, R. M. Finzi Neto, "Electromechanical impedance – based structural health monitoring instrumentation system applied to aircraft structures and employing a multiplexed sensor array", *J. Aerosp. Technol. Manag.* **7** (2015), no. 3, p. 294-306.

[5] R. Finzi Neto, V. Steffen Jr, D. Rade, C. Gallo, L. Palomino, "A low-cost electromechanical impedance-based SHM architecture for multiplexed piezoceramic actuators", *Struct. Health Monit.* **10** (2011), no. 4, p. 391-402.

[6] S. W. F. de Rezende, B. P. Barella, J. R. V. Moura Jr, K. M. Tsuruta, A. A. Cavalini Jr, V. Steffen Jr, "ISHM for fault condition detection in rotating machines with deep learning models", *J. Braz. Soc. Mech. Sci. Eng.* **45** (2023), article no. 212.

[7] A. Cavalini Jr, R. Finzi Neto, V. Steffen Jr, "Impedance-based fault detection methodology for rotating machines", *Struct. Health Monit.* **14** (2015), no. 3, p. 228-240.

[8] J.-W. Kim, C. Lee, S. Park, "Damage localization for CFRP-debonding defects using piezoelectric SHM techniques", *Res. Nondestruct. Eval.* **23** (2012), no. 4, p. 183-196.

[9] O. Cherrier, P. Selva, V. Pommier-Budinger, F. Lachaud, J. Morlier, "Damage localization map using electromechanical impedance spectrums and inverse distance weighting interpolation: Experimental validation on thin composite structures", *Struct. Health Monit.* **12** (2013), no. 4, p. 311-324.

[10] B. A. de Castro, F. G. Baptista, F. Ciampa, "New imaging algorithm for material damage localisation based on impedance measurements under noise influence", *Measurement* **163** (2020), article no. 107953.

[11] J. Zhu, X. Qing, X. Liu, Y. Wang, "Electromechanical impedance-based damage localization with novel signatures extraction methodology and modified probability-weighted algorithm", *Mech. Syst. Signal Process.* **146** (2021), article no. 107001.

[12] S. Sikdar, S. K. Singh, P. Malinowski, W. Ostachowicz, "Electromechanical impedance based debond localisation in a composite sandwich structure", *J. Intell. Mater. Syst. Struct.* **33** (2022), no. 12, p. 1487-1496.

[13] D. R. Gonçalves, J. R. V. Moura Jr, P. E. C. Pereira, "Monitoramento de integridade estrutural baseado em impedância eletromecânica utilizando o método de krigagem ordinária", *Holos* **36** (2020), no. 2, p. 1-16.

[14] D. R. Gonçalves, J. R. V. Moura Jr, P. E. C. Pereira, M. V. A. Mendes, H. S. Diniz-Pinto, "Indicator kriging for damage position prediction by the use of electromechanical impedance-based structural health monitoring", *C. R. Méc.* **349** (2021), no. 2, p. 225-240.

[15] R. Soman, S. K. Singh, P. Malinowski, "Damage localization using electromechanical impedance technique based on inverse implementation", *Struct. Health Monit.* **22** (2023), no. 5, p. 3373-3384.

[16] L. Wang, B. Yuan, Z. Xu, Q. Sun, "Synchronous detection of bolts looseness position and degree based on fusing electro-mechanical impedance", *Mech. Syst. Signal Process.* **174** (2022), article no. 109068.

[17] X. Fan, J. Li, "Damage identification in plate structures using sparse regularization based electromechanical impedance technique", *Sensors* **20** (2020), no. 24, article no. 7069.

[18] M. Richards, M. Ghanem, M. Osmond, Y. Guo, J. Hassard, "Grid-based analysis of air pollution data", *Ecol. Model.* **194** (2006), no. 1, p. 274-286.

[19] A. Martowicz, M. Rosiek, "Electromechanical impedance method", in *Advanced Structural Damage Dectection: From Theory to Engineering Applications* (T. Stepinski, T. Uhl, W. Staszewski, eds.), John Wiley & Sons, Chichester, 2013, p. 141-176.

[20] G. Park, H. Sohn, C. R. Farrar, D. J. Inman, "Overview of piezoelectric impedance-based health monitoring and path forward", *Shock Vibr. Dig.* **35** (2003), no. 6, p. 451-463.

[21] C. Liang, F. P. Sun, C. A. Rogers, "Coupled electro-mechanical analysis of adaptive material systems-determination of the actuator power consumption and system energy transfer", *J. Intell. Mater. Syst. Struct.* **8** (1997), no. 4, p. 335-343.

[22] S. Bhalla, C.-K. Soh, "Electro-mechanical impedance technique", in *Smart Materials in Structural Health Monitoring, Control and Biomechanics* (C.-K. Soh, Y. Yang, S. Bhalla, eds.), Springer, Berlin, 2012, p. 17-51.

[23] F. P. Sun, Z. Chaudhry, C. Liang, C. A. Rogers, "Truss structure integrity identification using PZT sensor-actuator", *J. Intell. Mater. Syst. Struct.* **6** (1995), no. 1, p. 134-139.

[24] V. Giurgiutiu, C. A. Rogers, "Recent advancements in the electromechanical (E/M) impedance method for structural health monitoring and NDE", in *Smart Structures and Materials 1998: Smart Structures and Integrated Systems* (M. E. Regelbrugge, ed.), vol. 3329, International Society for Optics and Photonics, SPIE, San Diego, 1998, p. 536-547.

[25] G. Matheron, "Principles of geostatistics", *Econ. Geol.* **58** (1963), no. 8, p. 1246-1266.

[26] G. Matheron, "Kriging, or polynomial interpolation procedures? A contribution to polemics in mathematical geology", *Trans. Canad. Inst. Min. Metal.* **70** (1967), p. 240-244.

[27] G. Matheron, *The Theory of Regionalized Variables and its Applications*, Les cahiers du Centre de Morphologie Mathématique de Fontainebleau, vol. 05, École Nationale Supérieure des Mines de Paris, Paris, France, 1971.

[28] G. Matheron, "The intrinsic random functions and their applications", *Adv. Appl. Probab.* **5** (1973), no. 3, p. 439-468.

[29] P. E. C. Pereira, M. N. Rabelo, C. C. Ribeiro, H. S. Diniz-Pinto, "Geological modeling by an indicator kriging approach applied to a limestone deposit in Indiara city – Goiás", *REM - Int. Eng. J.* **70** (2017), no. 3, p. 331-337.
[30] C. A. S. Oliveira, M. A. A. Bassani, J. F. C. L. Costa, "Application of covariance table for geostatistical modeling in the presence of an exhaustive secondary variable", *J. Petroleum Sci. Eng.* **196** (2021), article no. 108073.
[31] F. Ogunsanwo, V. Ozebo, O. Olurin, J. Ayanda, J. Coker, O. Sowole, B. Ogunsanwo, J. Olumoyegun, J. Olowofela, "Geostatistical analysis of uranium concentrations in North-Western part of Ogun State, Nigeria", *J. Environ. Radioact.* **237** (2021), article no. 106706.
[32] A. Tayebi, S. Kasmaeeyazdi, F. Tinti, R. Bruno, "Contributions from experimental geostatistical analyses for solving the cloud-cover problem in remote sensing data", *Int. J. Appl. Earth Obs. Geoinf.* **118** (2023), article no. 103236.
[33] J.-P. Chilès, P. Delfiner, *Geostatistics: Modeling Spatial Uncertainty*, 2nd ed., Wiley Series in Probability and Statistics, John Wiley & Sons, Hoboken, 2012.
[34] A. G. Journel, C. J. Huijbregts, *Mining Geostatistics*, Academic Press Limited, London, 1978.
[35] M. Abzalov, *Applied Mining Geology*, Springer International Publishing AG, Cham, 2016.
[36] A. J. Sinclair, G. H. Blackwell, *Applied Mineral Inventory Estimation*, Cambridge University Press, Cambridge, 2002.
[37] M. J. Pyrcz, C. V. Deutsch, *Geostatistical Reservoir Modeling*, 2nd ed., Oxford University Press, New York, 2014.
[38] M. Armstrong, *Basic Linear Geostatistics*, Springer, Heidelberg, 1998.
[39] E. H. Isaaks, R. M. Srivastava, *An Introduction to Applied Geostatistics*, Oxford University Press, New York, 1989.
[40] J. K. Yamamoto, P. M. B. Landim, *Geoestatística: Conceitos e Aplicações*, 1st ed., Oficina de Textos, São Paulo, 2013.
[41] M. E. Rossi, C. V. Deutsch, *Mineral Resource Estimation*, Springer Science+Business Media, Dordrecht, 2014.
[42] C. Lantuéjoul, *Geostatistical Simulation: Models and Algorithms*, Springer-Verlag, Heidelberg, 2002.
[43] J. Deutsch, M. Deutsch, R. Martin, W. Black, T. Acorn, R. Barnett, M. Hadavand, "Pygeostat", 2021, version 1.1.1, Centre for Computational Geostatistics, https://pypi.org/project/pygeostat/.
[44] M. J. Pyrcz, H. Jo, A. Kupenko, W. Liu, A. E. Gigliotti, T. Salomaki, J. Santos, "GeostatsPy Python Package", 2021, version 0.0.26, Texas Center for Data Analytics and Geostatistics, https://pypi.org/project/geostatspy/.
[45] A. Falade, J. Amigun, Y. Makeen, O. Kafisanwo, "Characterization and geostatistical modeling of reservoirs in 'Falad' field, Niger Delta, Nigeria", *J. Pet. Explor. Prod. Technol.* **12** (2022), p. 1353-1369.
[46] A. Ali, A. Farid, T. Hassan, "3D static reservoir modelling to evaluate petroleum potential of Goru C-Interval sands in Sawan Gas Field, Pakistan", *Episodes* **46** (2023), no. 1, p. 1-18.
[47] X. Wang, Q. Xia, "Depiction of different alteration zones using fractal and simulation algorithm in Pulang Porphyry Copper Deposit, Southwest China", *Nat. Resour. Res.* **31** (2022), p. 1943-1961.
[48] S. Karami, M. Jalali, A. Karami, H. Katibeh, A. Marj, "Evaluating and modeling the groundwater in Hamedan plain aquifer, Iran, using the linear geostatistical estimation, sequential Gaussian simulation, and turning band simulation approaches", *Model. Earth Syst. Environ.* **8** (2022), p. 3555-3576.
[49] S. Özen, C. Yesilkanat, M. Özen, A. Başsari, H. Taşkin, "Health risk assessment of soil trace elements using the Sequential Gaussian Simulation approach", *Environ. Sci. Pollut. Res.* **29** (2022), p. 72683-72698.
[50] P. Agyeman, L. Borůvka, N. Kebonye, V. Khosravi, K. John, O. Drabek, V. Tejnecky, "Prediction of the concentration of cadmium in agricultural soil in the Czech Republic using legacy data, preferential sampling, Sentinel-2, Landsat-8, and ensemble models", *J. Environ. Manage.* **330** (2023), article no. 117194.